Space Sci Rev (2018) 214:97
https://doi.org/10.1007/s11214-018-0532-3

ExoMars 2016 Schiaparelli Module Trajectory and Atmospheric Profiles Reconstruction

Analysis of the On-board Inertial and Radar Measurements

A. Aboudan[1] · G. Colombatti[1] · C. Bettanini[1] · F. Ferri[1] · S. Lewis[2] · B. Van Hove[3] · O. Karatekin[3] · S. Debei[1]

Received: 9 March 2018 / Accepted: 26 July 2018 / Published online: 6 August 2018

Abstract On 19th October 2016 Schiaparelli module of the ExoMars 2016 mission flew through the Mars atmosphere. After successful entry and descent under parachute, the module failed the last part of the descent and crashed on the Mars surface. Nevertheless the data transmitted in real-time by Schiaparelli during the entry and descent, together with the entry state vector as initial condition, have been used to reconstruct both the trajectory and the profiles of atmospheric density, pressure and temperature along the traversed path.

The available data-set is only a small sub-set of the whole data acquired by Schiaparelli, with a limited data rate (8 kbps) and a large gap during the entry because of the plasma blackout on the communications.

This paper presents the work done by the AMELIA (Atmospheric Mars Entry and Landing Investigations and Analysis) team in the exploitation of the available inertial and radar data. First a reference trajectory is derived by direct integration of the inertial measurements and a strategy to overcome the entry data gap is proposed. First-order covariance analysis is used to estimate the uncertainties on all the derived parameters. Then a refined trajectory is computed incorporating the measurements provided by the on-board radar altimeter.

The derived trajectory is consistent with the events reported in the telemetry and also with the impact point identified on the high-resolution images of the landing site.

Finally, atmospheric profiles are computed tacking into account the aerodynamic properties of the module. Derived profiles result in good agreement with both atmospheric models and available remote sensing observations.

Keywords Mars atmosphere · Entry probe · Data assimilation

✉ A. Aboudan
alessio.aboudan@unipd.it

1 CISAS Giuseppe Colombo, University of Padova, Via Venezia 15, 35131, Padova, Italy

2 The Open University, Walton Hall, Kents Hill, Milton Keyness, MK7 6AA, UK

3 Royal Observatory of Belgium, Ringlaan 3, 1180 Brussels, Belgium

1 Introduction

The ExoMars programme foresees two missions, the first one consisting of the Trace Gas Orbiter (TGO) plus the Schiaparelli Entry Demonstrator Module (EDM) launched in March 2016 and the second one featuring a landing platform and a rover (launch is planned for 2020) (Vago et al. 2015). On 16th October 2016, after six months of interplanetary cruise, the TGO delivered Schiaparelli in a ballistic trajectory toward Mars. Then, after successful entry and descent under parachute, Schiaparelli failed the terminal part of the descent and crashed on the Martian surface.

Schiaparelli has been designed as an Entry, Descent and Landing (EDL) demonstrator. The on-board sensors were selected to both characterize the module performances during EDL and to enable scientific activities.

The on-board sensor suite is composed by four pressure sensors located on the Front-Shield (FS), ten thermal plugs embedded on the Thermal Protection System (TPS) of both the Back-Shell (BS) and the FS, one calorimeter and one radiometer. These latter sensors were part of the CoMARS+ experiment (Gulhan et al. 2017).

The module was also equipped with a down-looking DEscent CAmera (DECA) to support the landing site characterization. The camera was configured to acquire a burst of fifteen low-resolution frames starting from the FS release.

Finally the module was provided with a sensor-suite aimed to characterize the atmospheric conditions at the surface called DREAMS (Dust Characterization, Risk Assessment, and Environment Analyser on the Martian Surface) (Bettanini et al. 2018; Esposito et al. 2018). The suite comprised sensors to measure atmospheric temperature, pressure, humidity, wind speed and direction, illumination conditions and to provide the first measurements of electric fields at the Martian surface.

Schiaparelli Guidance Navigation and Control (GNC) subsystem included the main computer (CTPU), one Sun Detection Sensor (SDS) located in the lander BS, one Miniaturized Inertial Measurement Unit (MIMU), three pairs of landing accelerometers (axial and radial, not used on the control loop) and one Radar Doppler Altimeter (RDA).

The GNC subsystem was responsible to guide the module through the Mars atmosphere and trigger all the EDL key events such as the detection of the interface point with the atmosphere, the parachute opening, the FS release, the BS release and finally the activation and cut-off of the thrusters during the final part of the descent and the touchdown.

Schiaparelli was designed to collect the data from the aforementioned sensors, store them on-board and transmit the data to the available relay orbiters only after the touch-down. Moreover, during all the EDL phases, the module sent also a small sub-set of the collected parameters in real-time using the UHF antennas (the antenna on the BS until separation, thereafter the antenna on the Surface Platform). The UHF carrier was recorded by ground stations on Earth and the real-time telemetry was received by TGO and Mars-Express orbiters; this data set is very limited but contains all the information needed to reconstruct the chain of events occurred during the EDL.

The analysis of all the EDL data for scientific purposes is the goal of AMELIA experiment (Ferri et al. 2018). The flight data have been used by AMELIA team to reconstruct the Schiaparelli trajectory and to derive the profiles of atmospheric density, pressure and temperature along the traversed path. This work describes the analysis performed on MIMU and RDA available data and presents both the used methodologies and the obtained results. Flight data were retrieved by AMELIA team from ESA EGOS Data Dissemination System (EDDS) and all the data will be publicly available through ESA Planetary Science Archive (PSA, URL: https://archives.esac.esa.int/psa/).

The following Sect. 2 provides an overview of the main mission events, Sect. 3 reports the main used reference frames and the available data set, Sect. 4 describes the preliminary processing of inertial data and contains a brief description of the anomaly that led to the crash of Schiaparelli on Mars. The method used to reconstruct the trajectory is described in Sect. 5, the definition of the initial state vector is detailed in Sect. 6, RDA data is presented in Sect. 7 and the data assimilation procedure is in Sect. 8. The reconstruction of atmospheric profiles is described in Sect. 9 and the determination of the winds can be found in Sect. 10. Finally the annexes report the dynamic model of the spacecraft and the error models used for the assimilation of radar data.

2 Key Mission Events

The first part of ExoMars mission composed by the TGO plus Schiaparelli was launched from Baikonour cosmodrome on 14th March 2016 and reached Mars on 19th October 2016. On 16th October Schiaparelli was separated from the TGO on a ballistic trajectory. The module woke-up from its hibernation state after about 72 hours, one hour before the expected Entry Interface Point (EIP) with the atmosphere.

The Entry Interface Point (EIP) with the atmosphere was detected by Schiaparelli on 19th October 2016 at 14:42:22 Coordinated Universal Time (UTC). This event was the beginning of the EDL sequence. The first part of the EDL was the hypersonic entry phase that lasted about 181 s as expected by simulations. The Parachute Drogue Deployment (PDD) has been commanded by the GNC computer at 14:45:23 as expected, then the FS has been Released (FSR) after about 41 s at 14:46:04. The BS was separated after a further 41 s at 14:46:46 (earlier than expected). Then the thrusters were activated at 14:46:50 but for only 3 s, after which the Surface Platform fell under gravity until surface impact. See Tolker-Nielsen (2017) for a summary of the anomaly.

3 Real-Time Data Set

Overview of the Input Data All the analysis performed in this work is based on the GNC data present in the real-time telemetry. GNC computer used MIMU data, supplemented after FSR from RDA data, to get the EDM rotation rate, attitude, acceleration, velocity, and position during the whole EDL sequence.

GNC outputs were generated at 100 Hz but only a sub-set of them were part of the real-time TeleMetry (TM): total acceleration, angular rate and attitude were at 10 Hz while module velocity and position were at 1 Hz.

Available data cover the time span from 14:22:43 to 14:46:58 corresponding to the time frame from about 20 minutes before the interface to 8 s after the thrusters activation. Samples are almost uniformly spaced with four data gaps caused by ionization blackout during the entry phase. Data gaps are respectively 1.4 s, 1.8 s, 3.3 s and 57.2 s long, from 14:42:45 to 14:43:53. A summary of the used data is reported in Table 1.

Finally RDA measurements of slant-out and slant-ranges are available between 14:45:05 and 14:46:49; their use to fix the EDM trajectory is described in Sect. 8.

Reference Frames and Altitude Definition We used three main reference frames. The inertial frame is the Mars Mean Equator and IAU vector of J2000 (MMED) as defined in the SPICE framework. The main body-fixed frame is called GNC frame, its center is located

Table 1 Summary of real-time telemetry data reporting inertial measurements, RDA data and EDM trajectory estimated on-board by GNC

Data	Start	Stop	Samples	Rate	Ref. frame
Angular rate	14:22:43	14:46:58	11174	10 Hz	GNC
Quaternion	14:22:43	14:46:58	11174	10 Hz	MMED to GNC
Total acc.	14:22:43	14:46:45	11129	10 Hz	MMED
Velocity	14:22:44	14:46:45	1108	1 Hz	MMED
Position	14:22:44	14:46:45	1108	1 Hz	MMED
RDA slant-range	14:46:28	14:46:38	2	0.1 Hz	GNC
RDA slant-out	14:45:05	14:46:49	399	10 Hz	GNC
RDA velocity-out	14:45:05	14:46:49	399	10 Hz	GNC

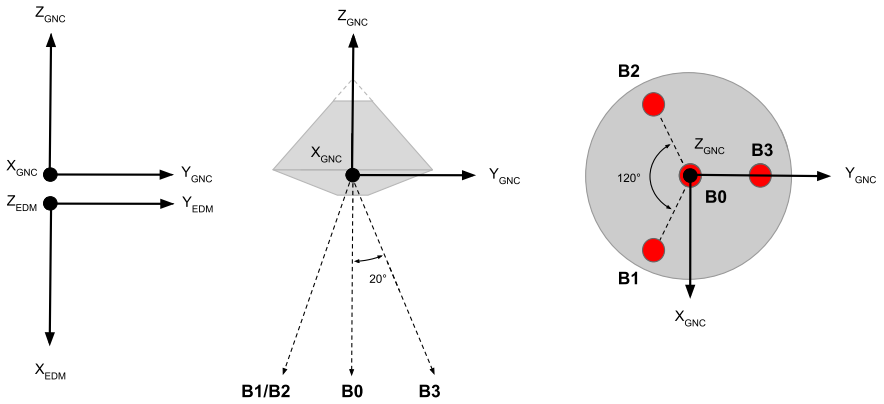

Fig. 1 GNC reference frame, EDM reference frame and the geometry of RDA beams

at the Centre of Gravity (CoG) of the module with the Z-axis aligned with the symmetry axis and pointing to the BS as shown in Fig. 1. A secondary body-fixed frame called EDM frame is used both to compute the aerodynamic forces and torques using the Schiaparelli aerodynamic database and to represent the local attitude; in particular pitch and yaw angles correspond to EDM Y and Z axes and to GNC Y and X axes. Finally the standard North East Down (NED) reference frame is used to define the position in terms of longitude and latitude as well as the roll, pitch and yaw attitude angles. The attitude transformation from the MMED frame to the GNC frame is represented using JPL quaternion parametrization (Shuster 1993). The spacecraft altitude Above MOLA Radius (AMR) is computed with respect to the constant MOLA radius of 3396 km, while the altitude Above Ground Level (AGL) is computed with respect to the mean terrain elevation at a specific position.

The GNC Estimated Trajectory The trajectory provided by GNC was based on the initial conditions preloaded on-board before the separation from the TGO. Position and velocity were determined propagating the TGO state before the separation to the expected wake-up time, while the attitude after the wake-up was estimated on-board using the SDS. This approach fulfills the needs of the GNC but does not take into account the post-flight knowledge. In particular the over-performances of Main Separation Assembly resulted in higher separation velocity and slightly steeper flight path angle with respect to values pre-

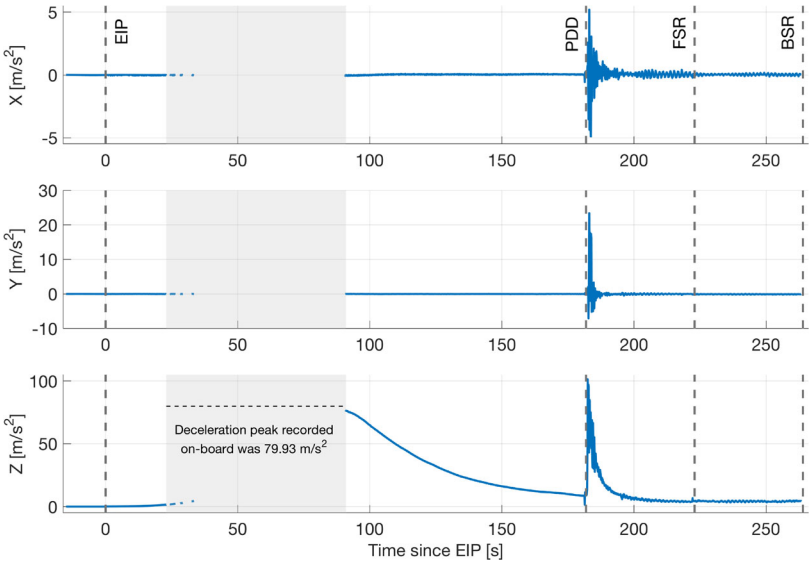

Fig. 2 Acceleration measured on-board and main EDL events. Entry interface point EIP event is used as reference time. Other events PDD, FSR and BSR are reported in the plots. It is evident the data gap due to plasma blackout from 23 s to 91 s after the EIP. After the gap the Z acceleration profile is consistent with the peak measured on-board of 79.93 m/s^2. At the PDD the parachute deployment resulted in a 101.5 m/s^2 acceleration peak along Z and in fast oscillations along X and Y axis

dicted by pre-EDL simulations. Moreover, post-flight data analysis evidenced a saturation of the X-axis gyroscope at the parachute deployment. The gyro saturation was caused by an angular rate exceeding the design threshold of about 187.5°/s, hence the lander attitude, velocity and position computed by the GNC after the PDD were wrong. In particular the error in the altitude, latter when RDA data was introduced in the control loop, caused the premature BS separation and activation of the thrusters (Bonetti et al. 2017; Portigliotti et al. 2017).

4 Preprocessing of GNC Data

Aerodynamic Acceleration The real-time telemetry contains the inertial acceleration computed by the GNC computer. First the GNC estimated position is interpolated and resampled at 10 Hz (see Table 1) then the gravitational acceleration is computed and removed to get the aerodynamic component; the used gravity field is JPL MRO120D model limited at order 2; the model is available from NASA Planetary Data System (PDS, URL: https://pds.nasa.gov). Finally the GNC attitude quaternion is used to transform the aerodynamic acceleration from inertial to body frame. This process removes also the effects of the wrong attitude provided by the GNC computer after PDD. Figure 2 shows the resulting body frame acceleration along X, Y and Z GNC axes correlated with the EDL events. The data gap due to plasma blackout is evident in the window from 23 s to 91 s after the EIP. The maximum deceleration recorded on board and reported in TM was 73.93 m/s^2 just before the end of the blackout. Then, at the PDD, the parachute inflation caused another peak along Z of about 101.5 m/s^2.

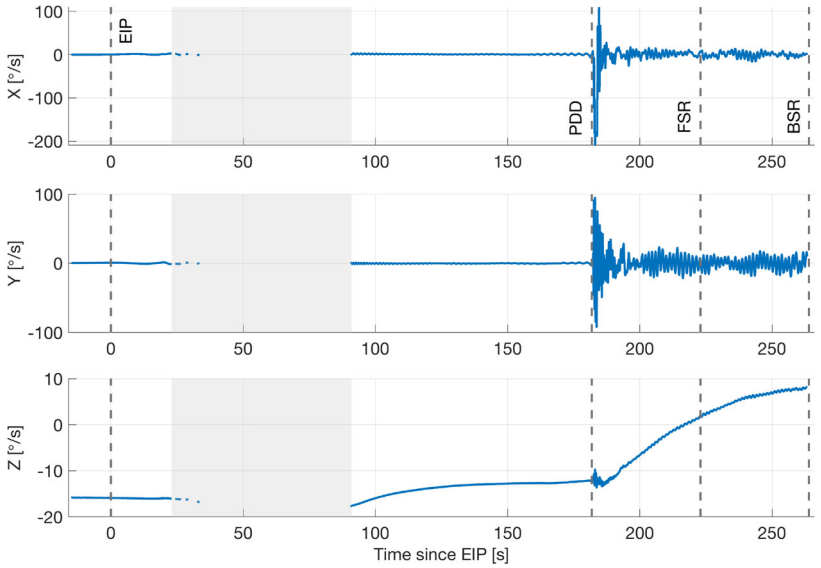

Fig. 3 Angular rate measured on-board and main EDL events. The Z angular rate during the entry shows a constant rotation of about 16°/s as expected from separation from TGO. After the black-out there is a reduction in the Z rate up to about 12°/s that could be related with some asymmetric ablation of the FS or to some drift in the navigation sensors. At the PDD the X angular rate exceeded the design threshold of 187.5°/s causing the saturation of the sensor

Angular Rate Data During the entry phase the Z angular rate in Fig. 3 shows a constant rotation at about 16°/s in line with the expected value from TGO separation. After the blackout there is a slight reduction of the rotation rate from 16°/s to about 12°/s and the Z angular rate profile seems correlated with the Z acceleration. This variation could be linked to some asymmetric ablation of the FS or it could be the effect of some drift in the navigation sensors (Bonetti et al. 2017). After the parachute deployment the angular rates show very fast oscillations mainly along X and Y axes for about 4 seconds. During the remaining part of the descent phase the angular rates show slow oscillations of the DM below the parachute and a torsional motion along Z axis.

Reconstructed Yaw Rate During Gyro Saturation The fast oscillations at parachute opening exceeded the threshold of 187.5°/s along X axis while they were well inside the design limit on Y axis. The X gyro saturation occurred 1 s after the PDD and lasted 1 s as shown in detail in Fig. 4.

The EDM oscillations during parachute inflation were linked to the parachute drag force applied along Z axis and measured on-board. The first peak on Z acceleration was about 0.6 s after PDD, from then on the acceleration decreased oscillating with a period of about 0.35 s. These oscillations are probably due to combined effects of canopy-bridle elasticity and canopy area oscillations that could occur when the parachute is deployed in supersonic regime (in this case around Mach 2).

The X gyro saturation is correlated with the second peak of the acceleration along Z, about 1 s after PDD (see Fig. 4). This suggest that the second peak on the acceleration could have been combined with the probe tilt resulted from the first peak causing an increased angular rate.

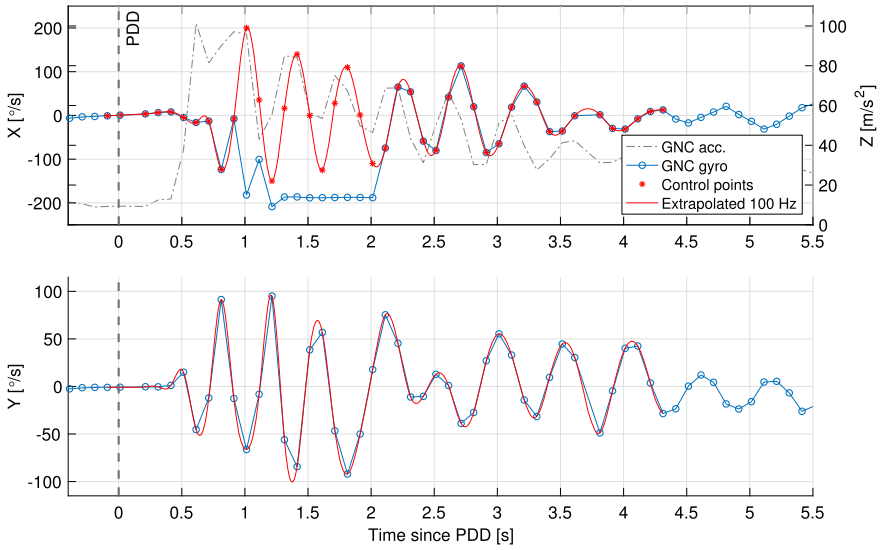

Fig. 4 X yaw and Y pitch angular rate reconstructed after gyro saturation, interpolated using a cubic function and resampled at 100 Hz

The X angular rate during saturation is then derived consistently with both the TM events and the Z acceleration profile following the best hypothesis formulated by other investigation (Bonetti et al. 2017).

Data Extrapolation During PDD Both acceleration and angular rate data are interpolated using piecewise continuous cubic function and resampled at 100 Hz during the first 5 seconds after the PDD event (about 190 s after EIP) to track the very fast oscillations that occurred at the parachute deployment.

5 Trajectory Integration

Forward Integration The EDM trajectory can be computed by numerical integration using the model detailed in Annex A. The EDM state is composed by inertial velocity, position and attitude quaternion in Eq. (A.1) and the corresponding equations of motion are reported in Eq. (A.2). The accelerations and rebuilt angular rates derived in Sect. 4 are used as input to the integration process. Gravitational force is modeled as a function of the EDM position using JPL MRO120D model limited at order 12; higher order harmonics does not change the results. The integration could be carried out using Euler method for velocity and position and a first-order quaternion integrator for the attitude (Wertz 1978) or alternatively using the classical fourth order Runge-Kutta method.

Handling Data Gaps For each gap in the TM we identify the last data sample before the gap (point a) and the first data sample after the gap (point b). Gaps are located in the entry part of the trajectory hence we can use the GNC attitude to compute the transformation from MMED to GNC for both the point a and b represented using the rotation matrices $\boldsymbol{C}_a$ and $\boldsymbol{C}_b$. Then we compute the velocity variation $\Delta\boldsymbol{v} = \boldsymbol{C}_a(\boldsymbol{v}_b - \boldsymbol{v}_a)$, the inertial position variation $\Delta\boldsymbol{p} = \boldsymbol{C}_a(\boldsymbol{p}_b - \boldsymbol{p}_a)$ and the attitude variation rotation matrix $\Delta\boldsymbol{C} = \boldsymbol{C}_b\boldsymbol{C}_a^T$ expressed

Table 2 Initial states defined at 14:42:07.125, 15 s before the detection of the atmosphere. The nominal state was defined according with the post-separation prediction of position and velocity plus the GNC attitude refined on-board. The refined state was identified by dispersion analysis to get the best consistency with RDA data and events timing. The optimal state is derived after RDA fixing by backward integration to the initial time. All the values are reported with 4 digits for numerical reasons independently from their uncertainty

Parameter	Unit	Field	Nominal	Refined	Optimal
Quaternion	N.A.	Q1	0.7250	0.7266	−0.7268
		Q2	−0.2476	−0.2549	0.2534
		Q3	0.3916	0.3884	−0.3858
		Q4	−0.5096	−0.5064	0.5087
Velocity	km/s	X	−4.9636	−4.9614	−4.9446
		Y	−3.3138	−3.3218	−3.3383
		Z	0.8326	0.8192	0.8178
Position	km	X	−1317.4056	−1315.3245	−1317.8932
		Y	3254.8625	3254.2178	3255.1296
		Z	−223.9034	−221.2223	−219.2404

using the body-frame at a. These values are then used during the integration process to derive the Schiaparelli state after the gap. To verify the performances of the method, the entry part of the trajectory was re-computed using an initial state retrieved from the on-board data. The integrated trajectory was then compared with the one computed by the GNC computer; the two trajectories were very similar with a maximum error in the velocity of 7.5 m/s, maximum position error of 530 m while the attitude quaternions were almost equal with an angular error lower than 0.01°.

First Order Covariance Analysis The uncertainties on both initial state vector and input measurements, are included in the trajectory integration by first order covariance propagation. The state vector is augmented adding the upper triangular part of the state covariance matrix and following the error state model in Eq. (A.15).

6 Initial State Definition

Nominal State Vector The initial state vector for the trajectory reconstruction is defined at 14:42:07.125 i.e. 15 s before the interface with the atmosphere. At this time the trajectory is purely ballistic and the atmospheric effects are considered negligible. The EDM position and velocity are then retrieved from the post-separation trajectory prediction provided by Thales-Alenia-Space that accounts for the separation mechanism performances measured on-board. Instead the attitude is retrieved from GNC TM data since the attitude quaternion was refined on-board using the SDS. The resulting state is reported in Table 2.

Refined State Vector Starting from the nominal state a dispersion analysis has been performed to identify the best initial state for the reconstruction. 10000 trajectories have been defined integrating on-board acceleration and angular rates with random initial state computed according with the dispersion parameters in Table 3. Very large variability ranges were selected to investigate almost all the dynamic conditions that can arise at the interface

Table 3 Parameters standard deviations used for the dispersion analysis around the nominal state and for the reconstruction of both the trajectory and the atmospheric profiles

Parameter	Unit	Dispersion analysis	Reconstruction
Attitude	°	5	1
Velocity	km/s	0.5	0.01
Position	km	10	2.0
Angular rate	°/s	N.A.	0.01
Angular rate at PDD	°/s	N.A.	10
Acceleration	m/s^2	N.A.	0.001
RDA slant-range	m	N.A.	100
RDA slant-out	m	N.A.	100
RDA velocity-out	m/s	N.A.	25
Wind speed[a]	m	N.A.	10
Axial and normal drag coeff.[a]	%	N.A.	10

[a]Used only for the determination of atmospheric profiles

with the atmosphere. This resulted in several trajectories that were not compatible with the available data, hence each generated trajectory was checked considering several parameters. To identify the most likely trajectories the following requirements were set:

- Mach number at PDD to be 2 ± 0.2
- PDD altitude to be 10 ± 2 km AMR
- FSR altitude to be 6 ± 2 km AMR
- Altitude at the end of the integration to be 3 ± 2 km AMR
- Time from the end of integration to the estimated impact to be 40 ± 15 s (this to be consistent with the TM events timing)

Only a sub set of the original trajectories satisfied all the requirements; Fig. 5 shows the valid trajectories with respect to the altitude parameters. Then the refined state was computed tacking the mean of the initial states of the selected trajectories. The difference between refined and nominal state are about 1° for attitude, 0.015 km/s for velocity and 3.5 km for position.

The standard deviation of the initial states of the selected trajectories was used to estimate the uncertainty of position, velocity and attitude to be used for the reconstruction step; values are reported in Table 3.

7 Analysis of Radar Measurements

RDA Data Overview The RDA was a Ka-band Radar Doppler Altimeter designed to support the determination of DM velocity and altitude with respect to the Mars surface during the landing phase (Bombaci et al. 2016). RDA was activated after FSR event and the real-time TM contains several data packets from 14:45:05 to 14:46:54. In this work we considered the slant-range, the slant-out and the velocity-out data. Slant-range packets contain four range measurements in meters along the four beams B0, B1, B2 and B3 reported in Fig. 1. The slant-out packets contain only one range measurement along the central beam

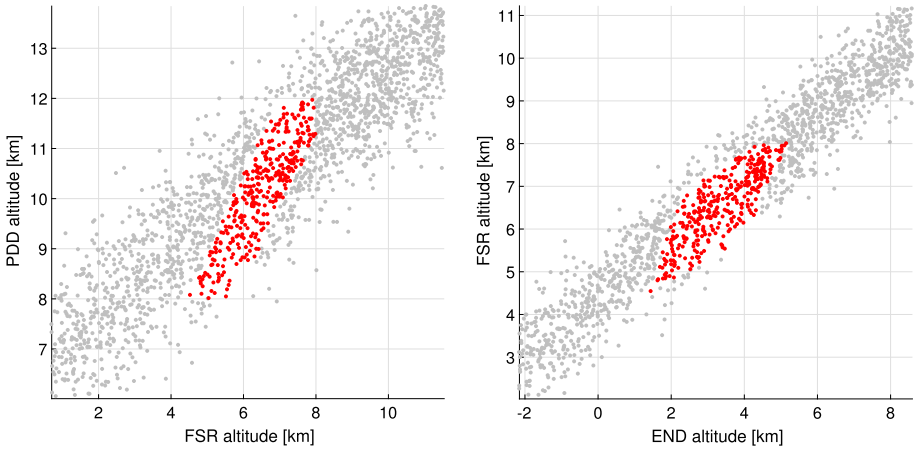

Fig. 5 Altitude AMR of PDD event, FSR event and the last integration point for the trajectories generated changing the initial state vector with the dispersion parameters in Table 3. Red dots correspond to the trajectories that were selected to get best consistency with available data, gray dots are the trajectories that were discarded from the analysis

Table 4 Altitude above the ground and off-vertical angle reconstructed using RDA slant-range data

Sample	UTC	B0 m	B1 m	B2 m	B3 m	Alt. AGL m	Off-vert. °
RDA3	14:46:28.363	5932.10	6515.18	6969.29	5563.50	5544.02	20.48
RDA4	14:46:38.363	4764.35	4966.60	5051.11	5237.19	4755.66	4.89

B0. The velocity-out packets contain the terrain relative velocity estimated using RDA range measurement and expressed with respect to the GNC frame. The used data are summarized in Table 1.

Slant-Range Processing Five slant-range packets are available, the first two were filled with 0 s, the last one was acquired after the end of the inertial data stream and hence only two packets called RDA3 and RDA4 have been used for the reconstruction. To correctly interpret the RDA data and model RDA measurements for data assimilation, we used the MOLA Mission Experiment Gridded Data Record (MEGDR) (Smith et al. 2001). Elevation data in a 5 km buffer around the impact point show a very flat terrain at 463 m scale length with mean elevation of −1440 m with respect to the MOLA reference radius. The slant-range data confirms that the surface close to the impact point was flat. For each packet, the four ranges were used to fit a plane (using a least square method) and then the Altitude above the Ground Level (AGL) was estimated tacking the distance from the centre of the GNC frame to the plane, while the off-vertical angle of the DM was computed as the angle between the GNC Z axis and the plane normal. The results are reported in Table 4.

Using the altitude AGL derived from RDA3 and RDA4 we can get a preliminary estimate of the altitude AGL profile, as the line passing through the two points, and of the descent velocity as $\Delta h_{\text{AGL}}/\Delta t = 78.9$ m/s.

Slant-Out Data Analysis Slant-out data corresponds to the measurement of the distance to the ground along the B0 direction sampled at 10 Hz. This data is correlated to the altitude AGL through the cosine of the off-vertical angle i.e. $h_{\mathrm{AGL}} = s_{\mathrm{B0}} \cos(\alpha)$, where s is the slant-range and α is the off-vertical angle. The slant-out profile is compared with the altitude AGL derived from slant-range in Fig. 8. Between 241 s and 257 s since EIP, the slant-out was higher than the altitude AGL estimated from slant-range data, corresponding to an off-vertical angle between 22° and 28°. Before and after this time interval, the slant-out was close to the altitude AGL and the off-axis was small. This suggests the existence of an horizontal wind field that tilted the DM for about 10 s in the altitude range between 5.9 km AGL (4.5 km AMR) and 4.7 km AGL (3.2 km AMR). See Sect. 10 for more details about estimated winds speed and direction.

Velocity-Out Data RDA provided also an estimate of the terrain relative velocity expressed in the GNC reference frame sampled at 10 Hz in the same time range of the slant-out data.

8 Data Assimilation

Algorithm Description Data assimilation is implemented using an Extended Rauch-Tung-Striebel smoother; an excellent description of this algorithm can be found in Särkkä (2013). This is a two stage algorithm, the forward pass corresponds to an Extended Kalman Filter, then a backward pass is performed to constrain the estimated trajectory on the full measurements data set. The state vector in Eq. (A.1) and its covariance have been propagated forward in time using state equation Eq. (A.2) and error equation Eq. (A.14) (see also Sect. 5). Measured acceleration and angular rate were used as inputs to the propagation process. Initial state vector is reported in Table 2. In the last part of the descent, when RDA data became available, the state is updated using the measurement equations Eq. (B.3) and Eq. (B.5). Stochastic observability for such a complex model is challenging hence we decided to simply constrain the state updates computed by the filter to lie along some predefined directions. The slant-range was used to update position and attitude (not velocity), position update was projected on the local vertical while attitude update was projected on the local horizontal plane because, assuming a planar surface, Eq. (B.3) is invariant for rotations along the local vertical direction. The same approach was used also for the slant-out data. Instead, the velocity-out was used to update only attitude and velocity (not position).

Tuning and Validation of the Method The implementation of the algorithm described above requires the specification of the uncertainties parameters in Table 3. To perform both the tuning and the validation of the method we took advantage of the trajectories already generated for the dispersion analysis described in Sect. 6.

The initial state vector was defined as the mean initial velocity, position and attitude of the selected maximum likelihood trajectories, then we used the maximum values of the standard deviations around the mean to setup the initial state covariance matrix.

The angular rate and acceleration uncertainties were defined assuming a standard navigation grade IMU (no Schiaparelli IMU specification were available). Moreover, the standard deviation of the X axis angular rate during the PDD was increased by three orders of magnitude to cope with the uncertainty related with gyro saturation.

RDA measurement uncertainty was defined empirically to guarantee the convergence of the reconstruction algorithm over a randomly sampled subset of the maximum likelihood

trajectories. The tuning of these parameters was performed on 100 trajectories: for each trajectory the simulated RDA measurements were generated, corrupted by noise and then used to reconstruct the trajectory starting from a perturbed initial state. Finally the true trajectory and the reconstructed one were compared by means of the RMS errors on the state parameters (for the attitude we used roll, pitch and yaw angles).

Derivation of the Optimal Trajectory The algorithm propagated the refined initial state till the first RDA valid measurement at about 238 s past EIP, in this time frame the state covariance grown unbounded. From 238 s till the last inertial sample at 263 s past EIP, the RDA data were used to improve the state estimate and reduce the uncertainties on altitude, attitude and vertical velocity (latitude and longitude are not fixed). The backward step of the algorithm provided the best estimate of the trajectory based on all the available data. Note that from 238 s to the initial point, where no RDA data is available, the smoothed trajectory is equivalent to the backward propagation.

The reconstructed trajectory was then shifted of about 1 km north-west to match the impact points identified on high resolution image HiRISE ESP_048041_1780. This rigid shift is compatible with the uncertainties in the reconstructed parameters and does not change the shape of the trajectory nor the velocity profiles.

The optimal initial state vector derived after the shift was then reported in Table 2 and compared with both the nominal and refined vectors. Velocity variation is < 35 m/s, attitude is $< 1^\circ$ while position variation is < 4.5 km and compatible with the errors on initial parameters. Finally, parameters not included in the state vector (e.g roll, pitch, yaw, longitude, latitude ecc.) and their variance were computed using the smoothed state. The reconstructed position, velocity and attitude profiles are shown in Fig. 6, the reconstructed ground track is shown in Fig. 7 while Table 6 reports the values of the main trajectory parameters for each EDL event.

Final Trajectory Final trajectory is in line with the pre-flight simulations made by the prime contractor Thales Alenia Space Italy (TAS-I) and provided to AMELIA for the validation of the reconstruction algorithms. The entry part of the final trajectory, from the EIP at 104.1 km AMR to the PDD at 9.4 km AMR, is about 578 km long from west to east, the attitude shows the probe spinning around Z GNC with slowly varying rate from 16°/s to 12°/s while the reconstructed angle of attack is $< 5.5^\circ$ and it is consistent with the one derived from acceleration ratio.

The descent part of the trajectory from PDD to FSR is about 4.4 km long directed from west to east. The FSR altitude is 5.9 km AMR, at this point the northward velocity is close to 0 m/s, the eastward co-rotating velocity is decreasing and crosses the 0 m/s after 12 s, this results in a hook shaped ground track shown in Fig. 7. The shape of the ground track provides the evidence of the presence of winds close to the surface as by the off-vertical tilt measured by the RDA.

The pitch angle of the EDM reference frame represents the inclination of the DM with respect to the local vertical. After PDD, the pitch angle went from about 0° (DM horizontal) to about -90° (DM vertical), moreover there are two bell-shaped attitude variations centered at about 230 s and 250 s after EIP (see Fig. 6). The latter one corresponds to the increased slant-out profile shown in Fig. 8 suggesting that also the first one could be related with an horizontal wind field that increased the off-vertical angle of the DM; the first attitude variation occurred before the RDA activation and no slant-out data is available.

The ground track in Fig. 7 is consistent with impact points identified on HiRISE images acquired after the Schiaparelli landing; the timing and position of all the main points are

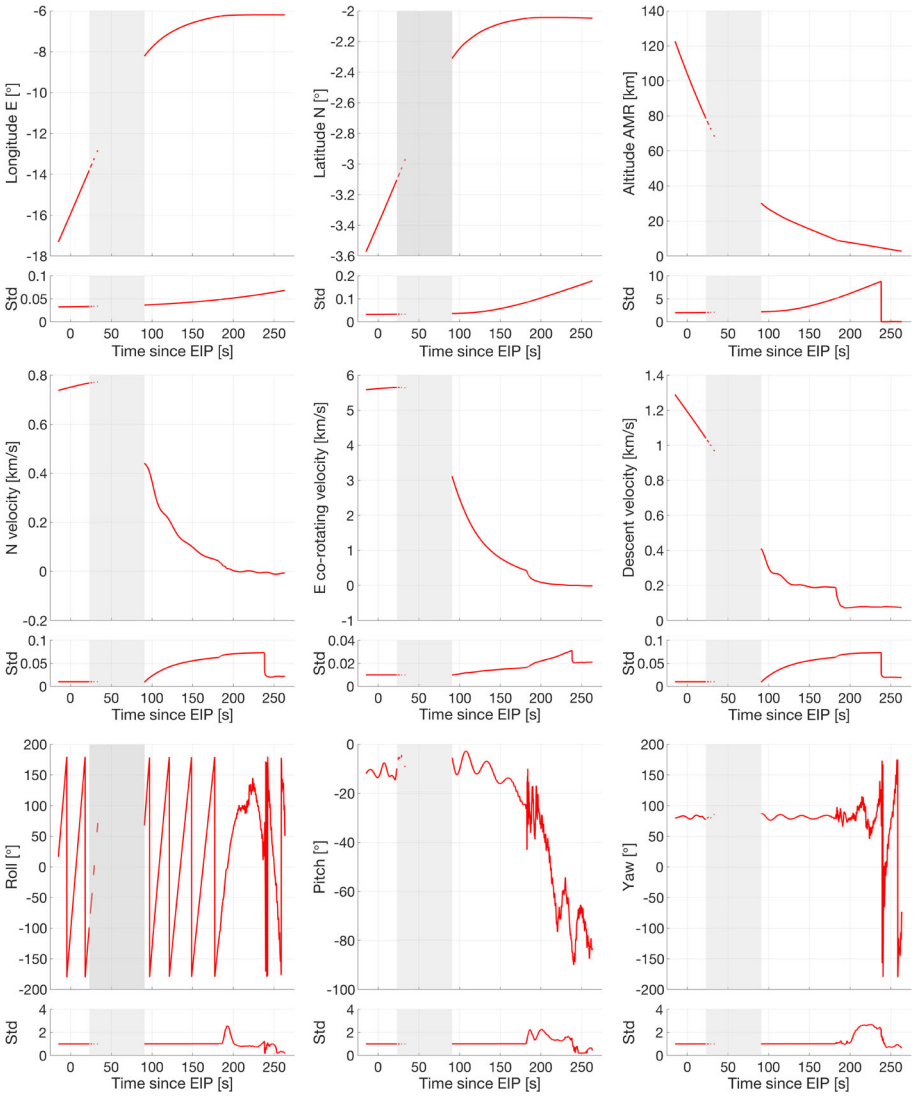

Fig. 6 Reconstructed latitude, longitude, altitude, terrain relative velocities and attitude. For each profile the standard deviation estimated by the smoother is reported; note the reduction of std. deviations produced by the RDA fix. The gray rectangle corresponds to the plasma blackout gap

reported in Table 5. The time from the end of the reconstruction to the impact at ground, computed simply by ballistic propagation of the last state till the ground level is about 33 s. This is compatible with the time tag of the last available TM packet corresponding to measurements made a short time before impact.

Goodness of Reconstructed Trajectory The reconstructed trajectory is compared with slant-range and slant-out data in Fig. 8. The reconstructed AGL altitude profile results in good agreement with estimates from RDA3 and RDA4 measurements. The reconstructed slant-range and slant-out match well the measurements with a maximum error < 150m.

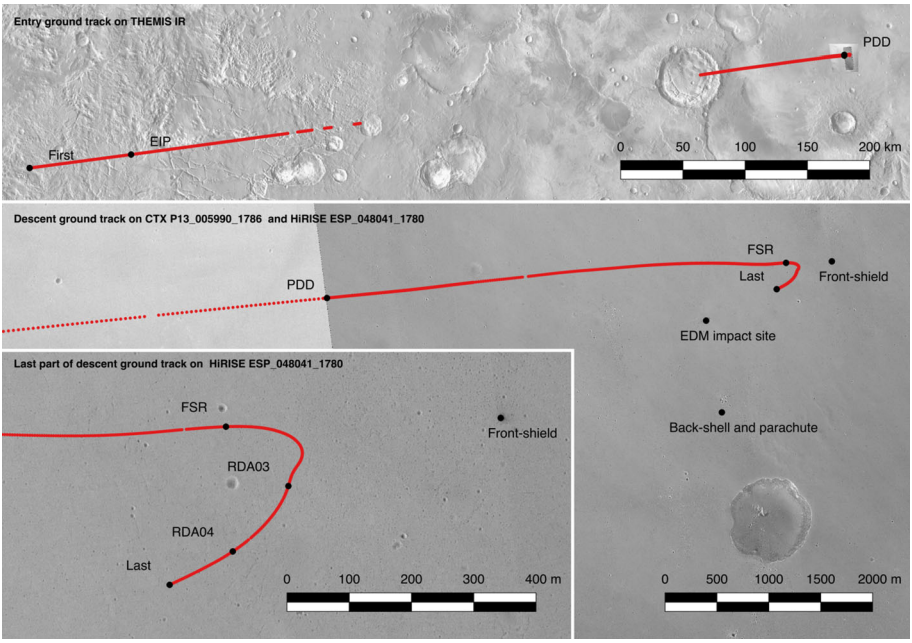

Fig. 7 Ground track of Schiaparelli on Mars surface. Black dots along the track correspond to the first trajectory point, the last trajectory point, the entry interface point (EIP), the parachute deployment (PDD), and the front shield release (FSR); numerical values can be found in Table 5. Gaps on the ground track (upper panel) correspond to missing data due to plasma blackout. The final part of the reconstructed ground track (mid panel) shows the compatibility with impact points of the different Schiaparelli elements identified on HiRISE. Both the hook shaped ground track and the position of the back-shell and parachute (bottom panel) are compatible with west, south-west wind fields below 9 km altitude AMR. NASA MGS THEMIS infrared maps, MRO CTX and HiRISE images were used as background depending on their footprint and resolution; data can be downloaded from NASA PDS

Table 5 List of positions of the relevant trajectory points by event and location of FS, BS and DM on the Martian surface

Name	Time UTC	Lon. E [°]	Lat. N [°]	Alt. AMR [km]
First data	14:42:07.125	−17.3091	−3.5723	122.6329
EIP	14:42:22.132	−15.9337	−3.3897	104.0366
Data gap begin	14:42:45.033	−13.8089	−3.1033	78.4935
Data gap end	14:43:52.733	−8.2191	−2.3111	30.1343
PDD	14:45:23.923	−6.2692	−2.0488	9.3871
FSR	14:46:05.135	−6.1946	−2.0430	5.9022
RDA3	14:46:28.341	−6.1929	−2.0446	4.0696
RDA4	14:46:38.337	−6.1944	−2.0464	3.2903
Last data	14:46:45.341	−6.1961	−2.0473	2.7630
FS location[a]	N.A.	−6.1872	−2.0428	−1.4420
DM impact site[a]	N.A.	−6.2076	−2.0524	−1.4440
BS and parachute[a]	N.A.	−6.2050	−2.0673	−1.4470

[a]Points measured on the Martian surface: longitude and latitude are identified on HiRISE ESP_048041_1780 image while altitude is derived from MOLA MEGDR

Table 6 Reconstructed local attitude, velocity, position and standard deviation of the main EDL events

Name	Unit	First	EIP	PDD	FSR	Last
Time	UTC	14:42:07.125	14:42:22.132	14:45:23.923	14:46:05.135	14:46:45.341
Roll	°	16.50 ± 1.00	-105.55 ± 1.00	-122.09 ± 1.01	123.05 ± 0.81	50.80 ± 0.18
Pitch	°	-12.03 ± 1.00	-13.50 ± 1.00	-26.41 ± 1.04	-70.77 ± 1.29	-83.19 ± 0.44
Yaw	°	79.88 ± 1.00	80.36 ± 1.00	81.54 ± 1.02	70.55 ± 2.66	-73.23 ± 0.63
Vel.	km/s	6.0219 ± 0.0173	6.0326 ± 0.0173	0.6950 ± 0.0907	0.2724 ± 0.1048	0.2390 ± 0.0170
FPA	°	12.36	11.41	15.74	16.73	18.12
HDA	°	82.79	82.70	86.39	89.85	−88.33
N vel.	km/s	0.7383 ± 0.0100	0.7512 ± 0.0100	0.0421 ± 0.0630	0.0007 ± 0.0725	-0.0066 ± 0.0219
E vel.	km/s	5.5867 ± 0.0100	5.6179 ± 0.0100	0.4263 ± 0.0163	0.0199 ± 0.0269	-0.0137 ± 0.0209
D vel.	km/s	1.2895 ± 0.0100	1.1930 ± 0.0100	0.1886 ± 0.0632	0.0784 ± 0.0727	0.0743 ± 0.0195
Lon. E[a]	°	-17.3091 ± 0.0326	-15.9337 ± 0.0329	-6.2692 ± 0.0482	-6.1946 ± 0.0571	-6.1961 ± 0.0685
	km	± 2.0049	± 2.0100	± 2.8656	± 3.3910	± 4.0662
Lat. N[a]	°	-3.5723 ± 0.0326	-3.3897 ± 0.0328	-2.0488 ± 0.0846	-2.0430 ± 0.1302	-2.0473 ± 0.1784
	km	± 2.0010	± 2.0064	± 5.0269	± 7.7295	± 10.5831
Alt. AMR	km	122.6329 ± 2.0000	104.0366 ± 2.0056	9.3871 ± 5.0513	5.9022 ± 7.7563	2.7630 ± 0.0390

[a]Longitude and latitude standard deviations are reported also in *km* for clarity

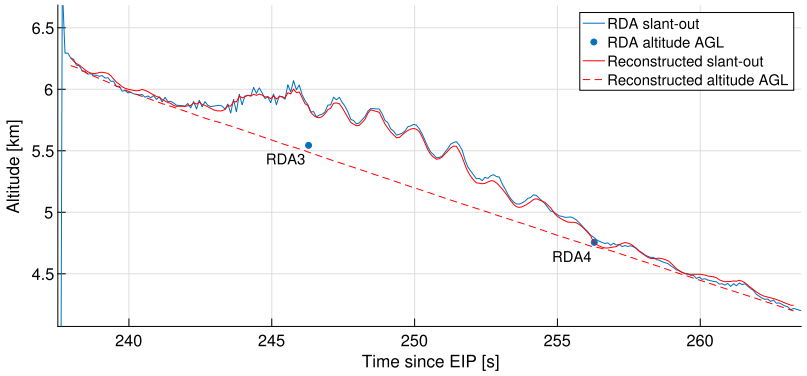

Fig. 8 Reconstructed altitude and slant-out compared with measured data during the last part of the descent phase. Reconstruction match well the measurements with maximum error < 150 m. The increased slant-out between 240 s and 260 s after EIP indicates an off-vertical tilt of the lander between 22° and 28° probably due to horizontal winds (see Sect. 10). The reconstructed altitude AGL is in good agreement with the one derived by slant-range data RDA3 and RDA4

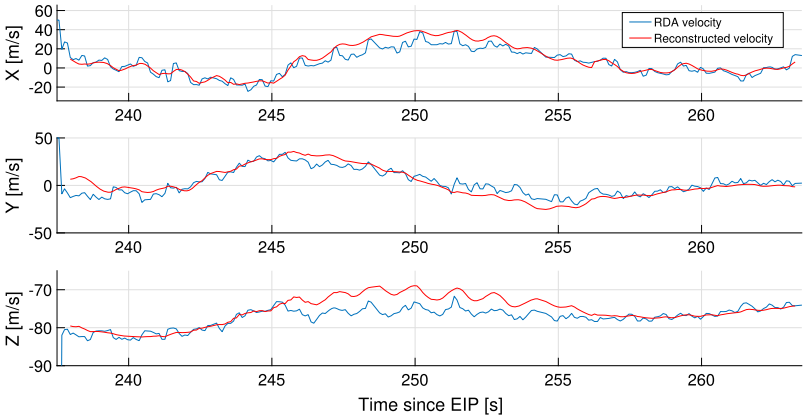

Fig. 9 Reconstructed velocity relative to the terrain (co-rotating) compared with the one estimated from RDA

Also reconstructed velocity-out is consistent with the measurements with a maximum error < 20 m/s as shown in Fig. 9.

Measurements residuals shown in Fig. 10 are zero mean, Gaussian distributed and well inside the uncertainty bounds even if the corresponding time series show some level of time correlation (they are not perfectly white noise). Slant-out residuals contain a periodic oscillation probably due with some un-modeled interaction between the parachute and the DM; error is relatively small and corresponds to a residual off-vertical inclination $< 5°$. Velocity-out residuals seem to be correlated with the off-vertical angle of the DM represented by the pitch in Fig. 6. Reducing the measurement uncertainty for slant-out and velocity-out could provide smaller and white residuals but the corresponding altitude profile is steeper resulting in un-realistic atmospheric profiles.

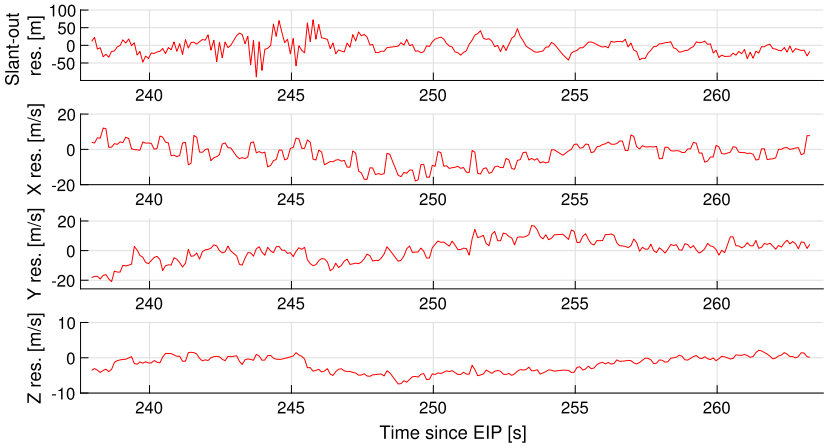

Fig. 10 RDA measurement residuals for slant-out and velocity-out

9 Reconstruction of the Atmospheric Profiles

Drag Equation The atmospheric drag measured on-board is directly related with the atmospheric density by the following equation

$$m\,a = \frac{1}{2}\,\rho\,v_r^2\,C\,A \tag{1}$$

where m is the mass of the spacecraft, a is the measured acceleration, ρ is the freestream atmospheric density, v_r is the probe speed relative to the atmosphere, C is the drag coefficient and A the reference area of the DM; the same equation holds for both axial and normal coefficients.

The relative velocity $v_r = \|\boldsymbol{v}_i - \boldsymbol{v}_s - \boldsymbol{v}_w\|$ is function of the inertial velocity $\boldsymbol{v}_i$, the surface velocity $\boldsymbol{v}_s$ and the wind velocity $\boldsymbol{v}_w$. The surface velocity is $\boldsymbol{v}_s = S(\boldsymbol{\omega})\boldsymbol{p}$ with S defined in Eq. (A.5), $\boldsymbol{p}$ the spacecraft position and $\boldsymbol{w}$ the Mars angular rate.

During the EDL, the Schiaparelli configuration changed several times. TAS-I provided both the spacecraft composite mass, inertia matrix and the aerodynamic parameters for each configuration expected during the EDL. In particular the Schiaparelli AErodynamic DataBase (AEDB) reported the axial and normal coefficients of the parachute and of the descent module. All the aerodynamic parameters are tabulated as a function of the Knudsen number, the Mach number and the angle of attack. Note that determination of Knudsen and Mach requires a reference atmosphere, to overcome this problem in deriving the atmospheric profiles a simple iterative method could be used (Blanchard and Desai 2011; Withers 2013).

Atmospheric Structure Reconstruction The reconstruction of the atmospheric density, pressure and temperature profiles is based on the inversion of Eq. (1). One very elegant method to simultaneously reconstruct the probe trajectory and the atmosphere structure is to augment the state vector in Eq. (A.1) adding the density and/or the pressure as state variables. This method was used both for ESA-NASA Huygens probe at Titan (Aboudan et al. 2008) and more recently for NASA Mars Science Laboratory (Karlgaard et al. 2014) with good results. Density evolution can be modeled using a Gauss-Markov process (Aboudan

et al. 2008) or by means of the hydrostatic equation and the perfect gas law (Karlgaard et al. 2014). Then the reconstruction is performed by means of a Bayesian filter (or smoother) algorithm using the measured acceleration both for the state propagation and for the measurement update step. The relation between pressure, density, temperature and altitude is often based on isothermal atmosphere assumption which holds only for small changes in altitude between consecutive measurements. As a consequence this approach requires a continuous stream of measurements at a suitable rate.

More often, the trajectory and atmosphere reconstruction are addressed separately, using the trajectory as an input to the atmosphere reconstruction. This approach was applied to Huygens (Kazeminejad et al. 2007; Colombatti et al. 2008), Mars Pathfinder (Spencer et al. 1999; Magalhães et al. 1999), Mars Exploration Rovers (Withers and Smith 2006), Phoenix probe (Blanchard and Desai 2011; Withers and Catling 2010; Withers 2013) and MSL (Chen et al. 2014; Holstein-Rathlou et al. 2016). In spite of what was actually planned by AMELIA (Ferri et al. 2018) and because of the limited data set, in this work, to cope with the plasma blackout and the low data rate we used this second approach.

Entry Atmospheric Structure Density is derived from Eq. (1) considering the GNC Z axis acceleration and the axial drag coefficient. During the entry, from 104 km to 9.4 km altitude, this results in the following equation

$$\rho = \frac{2\, m_{\mathrm{D}}\, a_{\mathrm{Z}}}{v_r^2\, C_{\mathrm{D}}\, S_{\mathrm{D}}} \tag{2}$$

where D stands for Descent module. To handle the data gap from about 70 km to 30 km altitude, a first estimate of the density was computed assuming zero wind speed and a constant $C_{\mathrm{D}} = 1.65$. This value for the drag coefficient was derived as the mean value of the C_{D} in the time span from the deceleration peak to the chute deployment on 500 runs of Monte Carlo entry simulation.

The density during the plasma black-out was then interpolated using an exponential function with altitude step of 10 m. Given the density profile, the pressure P was derived integrating the hydrostatic equilibrium equation along the trajectory

$$\frac{dP}{dh} = -\rho\, g_h \tag{3}$$

with h the altitude and g_h the radial component of the gravitational acceleration (the centrifugal terms were assumed negligible). The integration required an initial value for the pressure, we set $p_0 = 7\,10^{-3}$ Pa at $h_0 = 104$ km AMR according to the engineering model of the atmosphere. Then the temperature T was calculated using the ideal gas equation

$$T = \frac{P\, M}{\rho\, k_{\mathrm{B}}\, N_{\mathrm{A}}} \tag{4}$$

with M the mean molar mass of the Martian atmosphere, k_{B} the Boltzmann constant and N_{A} the Avogadro constant. The mean molar mass was set to $M = 43.41$ g/mol and assumed constant below 104 km according with Magalhães et al. (1999).

To get a refined atmospheric profile, the process described above was repeated in a loop using the C_{D} derived from the AEDB instead of a constant value (see Eq. (2)). For each point of the trajectory, the Knudsen and Mach numbers were computed using the atmospheric profiles at the previous iteration, the relative velocity and the angle of attack were derived from the reconstructed trajectory assuming again zero winds and finally, the refined C_{D} was

computed form the AEDB tables by simple bilinear interpolation. The termination condition was a relative variation below 1%, between successive iterations, on density, pressure and temperature; in this work three iterations were sufficient for convergence.

Descent Atmospheric Structure After the PDD event, the effects of the parachute must be taken into account. Analysis of accelerometer data showed that, after the very fast oscillations at parachute deployment, the relative angle between the parachute and the GNC Z axis of descent module was small ($< 5°$). Hence, assuming that the descent module and the parachute were aligned, the joint parachute-probe drag equation can be simplified as follow

$$\rho = \frac{2\,(m_{\mathrm{D}} + m_{\mathrm{P}})\,a_{\mathrm{Z}}}{v_r^2\,(C_{\mathrm{D}}\,S_{\mathrm{D}} + C_{\mathrm{P}}\,S_{\mathrm{P}})} \tag{5}$$

where D stands for Descent module and P for parachute.

Using Eq. (5), the atmospheric profiles during descent can be computed with the same method used for the entry. The main difference is that, at the first iteration, the C_{D} was derived from the AEDB instead of assuming a constant value using the atmospheric parameters from Mars Climate Database (MCD) climatology scenario (Millour et al. 2015). Also for the descent phase three iterations were sufficient to have a relative variation on the profiles below 1%.

Uncertainty on Atmospheric Profiles The standard deviation of density, pressure and temperature profiles were derived by first order covariance analysis using the covariance of the optimal trajectory and the parameters in Table 3. The uncertainty of the wind speed was set according to the dispersion of wind between different atmospheric scenarios at altitudes below 30 km; at higher altitudes the effects of winds are negligible with respect to the DM speed. For the drag coefficients we considered twice the maximum uncertainty reported on the AEDB to cope with unmodelled dynamics of both DM and parachute. Resulting 1σ bounds are shown in the detail plots of Figs. 12, 13 and 14.

Reconstructed Atmospheric Profiles The reconstructed profiles in Fig. 11 cover the altitude range from 104 km AMR to 2.8 km AMR. The plots show both raw profiles directly derived from acceleration data and refined profiles obtained smoothing the density and then recomputing pressure and temperature.

During the plasma blackout the density was extrapolated using an exponential model. The resulting profiles from 70 km AMR to 30 km AMR are in good agreement with the data below 30 km AMR confirming that the extrapolation does not introduce artefacts.

The temperature profile presents several high frequency oscillations on the upper atmosphere above 80 km AMR related with signal to noise ratio in the sensed acceleration. High frequency components are present also after PDD, i.e. below 9.5 km AMR and are related with unmodelled dynamics of the parachute-probe system.

The atmospheric profiles are compared with the available models of Mars atmosphere derived at the time of the EDL. The reference profiles were derived using MCD (Forget et al. 1999; Millour et al. 2015); MCD was used also to generate engineering models of the atmosphere during the design of Schiaparelli EDL system. Several different atmospheric scenarios are available in the MCD, in this work we considered the most general cases named climatology, warm, cold and dust, without perturbations. Moreover three assimilated profiles have been produced at the Open University, using a Global Circulation Model (GCM) properly modified to ingest the Mars Climate Sounder (MCS) data corresponding to Mars years with environmental conditions similar to that encountered by Schiaparelli.

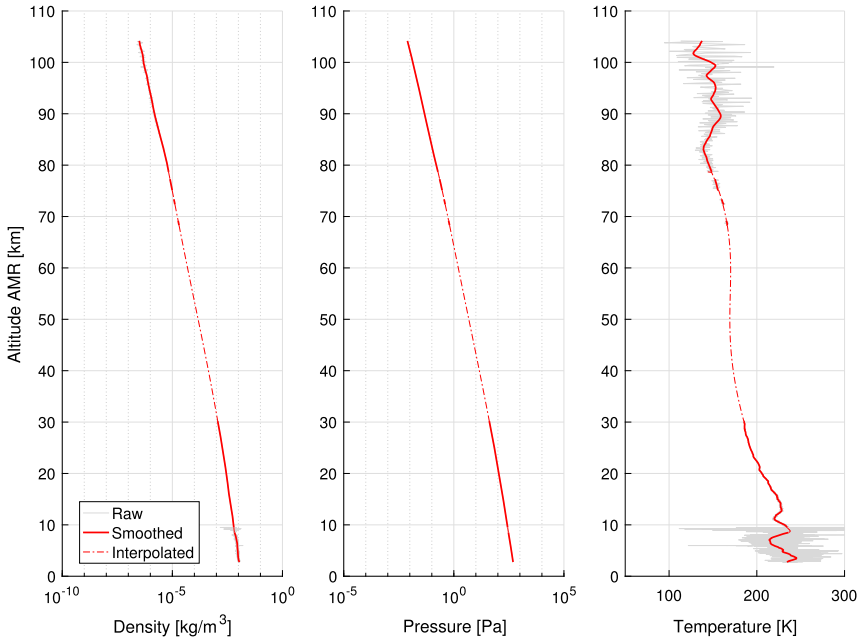

Fig. 11 Reconstructed free-stream density, pressure and temperature in function of the altitude. Data extrapolated during plasma blackout in the altitude range from 70 km AMR to 30 km AMR is consistent with the profiles before and after the blackout, no artifacts have been introduced

These profiles have been named MY24, MY25 and MY26 corresponding to the relevant Mars years.

Model profiles have been generated along the vertical at the center of the landing site and at the time of Schiaparelli EDL. They have been compared with refined profiles considering the relative variation of the reconstructed parameters R with respect to the model parameters M defined as $\delta_v = 100\,(v_R - v_M)/v_M$, the results are summarized in Table 7.

Entry Atmospheric Structure Before the Blackout Reconstructed atmospheric profiles before the blackout, from 104 km AMR to about 70 km AMR, are in good agreement with MCD climatology, MCD warm, MY24 and MY26 profiles as shown in Fig. 12. The best matching is with MY24 and MCD war profiles, resulting in relative variations on all parameters respectively $< 12.5\%$ and $< 15\%$.

Note that the refined temperature profile shows several oscillations above 80 km that could be related with zonal changes in the atmospheric structure because, between 104 km and 70 km AMR, horizontal translation of Schiaparelli was about 180 km. These variations are not present in the model profiles which were extracted along the vertical at the landing site center as averaged conditions with no atmospheric perturbations.

Entry Atmospheric Structure After the Blackout Entry phase atmospheric structure after the blackout extends from 30 km AMR to the PDD at 9.4 km AMR (Fig. 13).

The best matching before the PDD is with MY24 and MY26, the relative variation is $< 8.1\%$, and with MCD climatology, the relative variation is $< 11.7\%$.

Refined density from 30 km AMR to about 14 km AMR is in general higher than all the models (up to 17.4 %). In the altitude range between 13 km AMR and 10 km AMR, density

Table 7 Minimum and maximum relative variation (in %) of the reconstructed atmospheric profiles with respect to the models

Parameter	Model	Entry before blackout		Entry after blackout		Descent	
		min	max	min	max	min	max
Density	MCD clim.	7.31	40.26	−0.60	11.70	−1.34	11.47
	MCD dust	−75.38	−58.05	1.92	13.18	2.53	18.21
	MCD cold	53.56	89.32	−3.52	17.37	−4.30	8.00
	MCD warm	−14.80	15.01	0.95	12.37	0.42	13.85
	MY24	−5.73	12.49	−1.60	8.14	−4.88	8.31
	MY25	−23.73	−10.81	0.20	9.64	−3.47	10.45
	MY26	2.25	20.85	−2.97	8.02	−6.36	6.37
Pressure	MCD clim.	14.16	41.46	3.96	9.32	3.49	7.15
	MCD dust	−73.86	−64.74	−18.29	3.93	2.44	7.30
	MCD cold	60.28	88.19	4.51	23.50	2.85	6.84
	MCD warm	−10.79	13.05	−2.69	6.65	3.02	7.01
	MY24	−3.61	2.12	1.62	4.36	1.18	2.09
	MY25	−22.80	−17.92	−4.74	3.00	2.18	3.34
	MY26	6.44	12.10	1.24	6.01	0.31	1.29
Temperature	MCD clim.	−6.49	11.63	−3.16	4.35	−5.64	4.64
	MCD dust	−16.14	15.47	−20.30	−3.29	−11.56	1.43
	MCD cold	−8.23	8.78	2.59	9.25	−2.62	8.31
	MCD warm	−9.79	11.09	−9.68	2.09	−7.78	2.33
	MY24	−12.35	5.27	−4.56	3.32	−6.43	6.58
	MY25	−10.60	6.17	−10.16	2.14	−7.26	6.35
	MY26	−10.50	8.81	−2.20	4.16	−5.32	7.30

shows a sudden increase and inversion. This is confirmed independently by an increase on the raw output of pressure gauges located on the FS. Hence this inversion is likely to be related to an atmospheric feature.

Descent Atmospheric Structure The descent part of the atmospheric profiles cover the altitude range from 9.4 km AMR to 2.8 km AMR (Fig. 14).

The reconstruction of the atmospheric structure under parachute, using only acceleration data, is challenging because of the very high sensitivity of the atmospheric density to the parachute probe coupled dynamics. Moreover, the very high oscillations in density profile at parachute opening and high frequency components during the descent suggest some unmodeled dynamics of the probe-parachute system.

To remove the unrealistic changes in density due to instabilities at PDD, the density profile was interpolated using an exponential function in the altitude range from 9.4 km AMR to 8.5 km AMR.

The spike on both density and temperature well visible at 5.9 km AMR is due to FSR event and is not an atmospheric feature. Moreover the high frequency oscillations at a scale length about 90 m, are directly correlated with oscillations on the Z axis acceleration and most likely caused by areal effects of the parachute. These components were removed from the density profiles by a simple smoothing process.

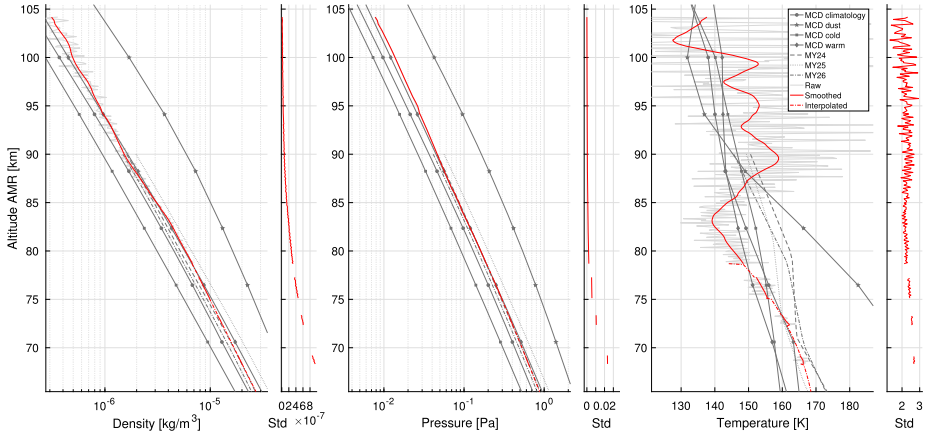

Fig. 12 Density, pressure, temperature and the corresponding standard deviations versus altitude for the entry phase before the plasma blackout

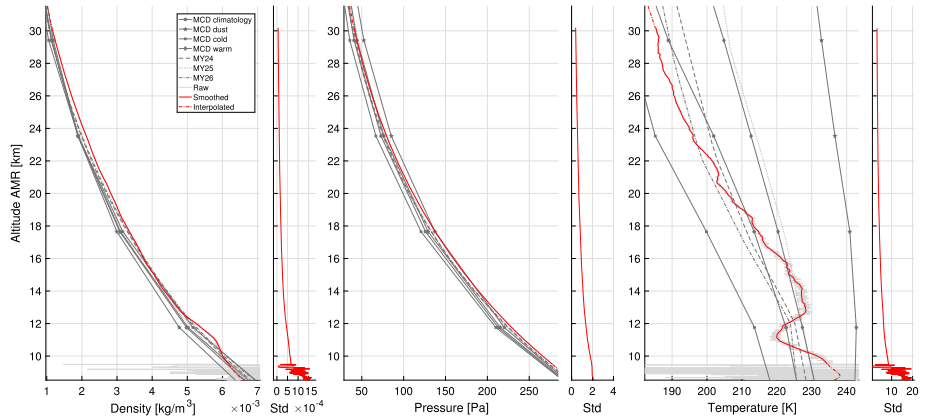

Fig. 13 Density, pressure, temperature and the corresponding standard deviations versus altitude for the entry phase after the plasma blackout

After the PDD and during the descent phase, the best matching is with MY26, the relative variation is $< 7.3\%$, and with MY24 and MCD cold profiles, the relative variation is $< 8.3\%$, even if the profiles are in good agreement with all the models, maximum relative variation is $< 18.2\%$.

The atmospheric structure is, in general, in good agreement with the models and the maximum relative variation is $< 18.2\%$. Moreover there are some structures at finer scale lengths (< 10 km) that are not resolved in the reference profiles. In particular, the smoothed profile during the descent phase shows an inversion between 9 km AMR and 3.5 km AMR plus the beginning of another inversion below 3.5 km AMR. To investigate the extent and shape of these profiles variations, the reconstruction uncertainty must be considered.

After the PDD the standard deviation of the atmospheric parameters increase and became huge. The low velocity and high density results in very significant sensitivity of the density to the relative speed of the DM. In particular density variations are correlated with velocity

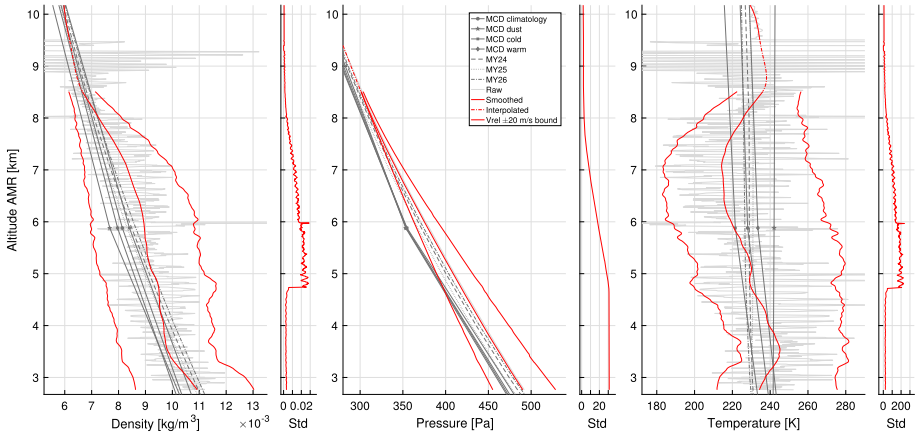

Fig. 14 Density, pressure, temperature and the corresponding standard deviations versus altitude for the descent phase. Raw and smoothed profiles are reported together with the boundaries relative to a variation of the reconstructed velocity of ± 20 m/s

variations by the following equation

$$\frac{\partial \rho}{\partial v_r} = -\frac{\rho}{v_r} \tag{6}$$

this term increases as the velocity decreases and density increases. As a consequence, during the final part of the descent, small changes in the velocity result in great density variations. As an example, after FSR the mean value of the term in Eq. (6) is about $1.4e^{-4}$ kg s/m^4 and hence a change of 20 m/s corresponds to a density variation of $2.8e^{-3}$ kg/m^3 and to a relative variation between the 28% and the 40% of the density estimate below 8 km AMR. Note also that the standard deviation of the reconstructed velocity ranges from 20 m/s to 80 m/s with the minimum value after the radar fix. This is reflected in the standard deviation of density, pressure and temperature indeed, to put in evidence the uncertainty and the variability in this parameters, Fig. 14 reports also the profiles corresponding to velocity changes of ± 20 m/s with respect to the reconstructed one.

10 Derivation of Wind Profiles

Evidence of Winds Before PDD, the DM speed was high and the effects of winds on the relative velocity could be considered negligible. At the PDD the Schiaparelli velocity decreased significantly, from 480 m/s to 80m/s (see Fig. 6), becoming comparable with winds speed expected at that altitude levels.

Effects of winds during the descent are evidenced by the hook shaped trajectory (see Fig. 7). Moreover the reconstructed pitch angle shows two bumps in the last part of the descent suggesting the existence of some wind fields that caused an off-vertical inclination of the DM. In particular the last bump from 245 s to 255 s after EIP is correlated with both the increase of the RDA slant-out and the increase of the DM off-vertical angle estimated by slant-range data (more details are reported in Sect. 7).

Wind Speed Estimation The atmospheric density and the presence of winds influence directly the drag force and the acceleration measured on-board.

To provide an estimate of the wind speed, the reconstructed co-rotating velocity of the DM was projected on the local frame and the north and east components of the acceleration were computed using a derivative filter (Fig. 15).

In the early part of the descent the horizontal acceleration tend to zero as an effect of the drag force; mainly on the E component. Small oscillations on both N and E direction with the same phase and 1.2 s period are not of atmospheric origin and are be caused by the parachute dynamics.

Moreover, to separate effects of density changes from wind speed, we assume that the variations in atmospheric density occur on length scales greater than the changes of local wind speed.

Remaining non-zero accelerations are then an indication of the presence of winds. The relation between wind speed and the horizontal acceleration and velocity is indeed complicated by the lander-parachute dynamics. Effects of changes on wind speed reflect on the horizontal acceleration and velocity with some lag depending on the characteristic response time of the lander-parachute system (Seiff 1993). To keep into account these and other effects we took advantage of a 9 DoF model of the DM linked to the parachute by a spherical joint. This model was developed by AMELIA team to support the design and test of the reconstruction algorithms and was validated using some reference simulations provided by the prime contractor.

The model was feed with the reconstructed state of the DM assuming that the parachute is aligned with the Z GNC axis. This assumption is not valid during the first part of the descent i.e. from 180 s to about 190 s after EIP because of the high oscillations at PDD while it is compatible with the accelerations sensed on-board in the remaining part of the descent.

The DM dynamic model uses both the AEDB and the reconstructed atmospheric profiles to predict the forces acting on the system. Predicted local accelerations were computed setting the wind speed to 0 m/s and were compared with the reconstructed accelerations in Fig. 15. The difference between predicted and reconstructed profiles is related to the wind effects. The predicted profiles are then recomputed iteratively adding winds with a speed proportional to this difference. The proportionality coefficient was increased at each iteration to reduce the RMS error between predicted and reconstructed acceleration below the 5%.

Wind Speed Profiles The wind profiles estimated with this procedure are reported in Fig. 16. Two horizontal wind fields with direction west/south-west were identified between 6 km and 5 km AMR and between 4.4 km and 3.2 km AMR, the maximum wind speed was about 20 m/s. Note that this value is quite higher than the one predicted by the MCD models without perturbations (about 10 m/s). Indeed the effects of small scale perturbations and factors other than general circulation should be taken into account in order to assess a realistic value.

11 Summary and Conclusions

We have presented the analysis of inertial and radar data received from Schiaparelli EDM during its entry and descent through the Martian atmosphere on 16th October 2016. The reconstructed trajectory is consistent with the timing of the mission events recorded in TM,

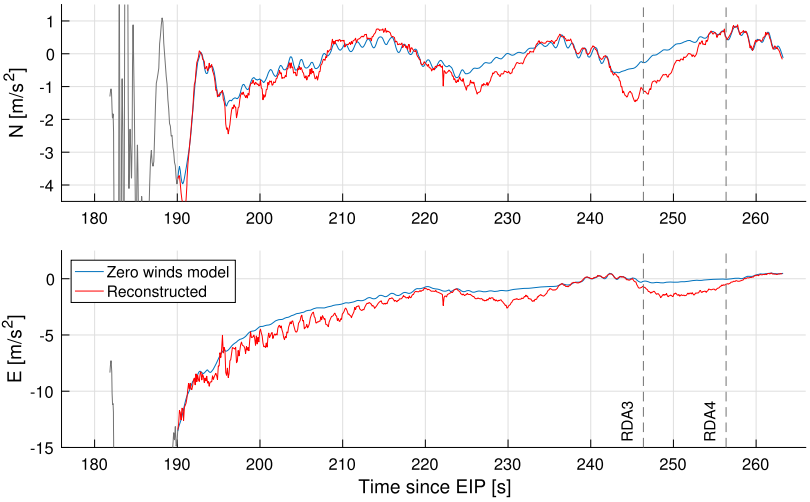

Fig. 15 North and east reconstructed acceleration compared with the acceleration predicted by a model with 0 m/s winds

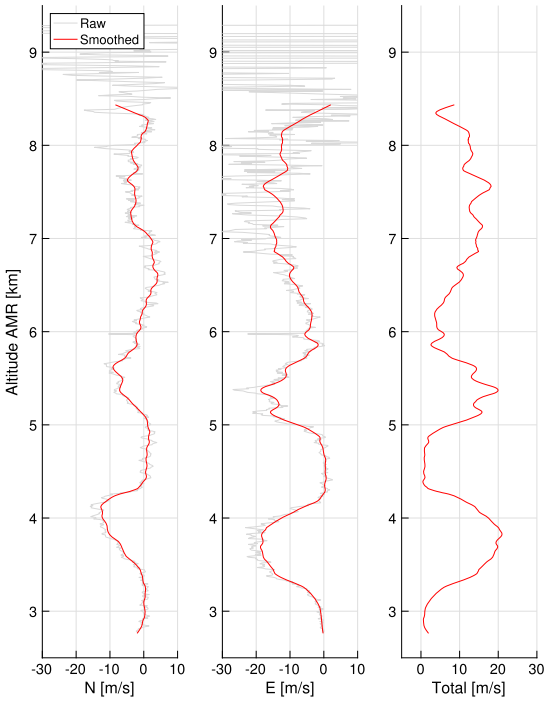

Fig. 16 North and east components of the wind speed estimated during the last part of the descent. The resulting horizontal wind is directed almost toward W, S-W with a maximum speed of 20 m/s

with the RDA data and with the impact points identified on high resolution images of the landing site. Corresponding atmospheric profiles are in good agreement with the available models of the Martian atmosphere.

Our analysis was based on the very limited telemetry transmitted by Schiaparelli in real-time during the EDL and it was challenging for several reasons. We developed a methodology to retrieve the on-board acceleration in the GNC reference frame, to fill the data gap during the black-out and to extrapolate the X axis angular rate during the gyroscope saturation at PDD. The approach was validated replicating the trajectory computed by the GNC sub-system with an error well inside the uncertainty in the input parameters.

The initial state, needed to reconstruct the trajectory, was derived starting from the on-board data and checking the consistency of the associated trajectories with respect to several parameters e.g. velocity profile, altitude profile and impact points to select the best hypothesis and to discard unrealistic trajectories. This step was crucial also to assess the uncertainty in both the initial state and the uncertainty parameters needed to tuning the data assimilation algorithm based on Bayesian smoothing. To include radar data in the analysis a custom model of DM, parachute and RDA measurements was developed and validated from scratch. Then an optimal trajectory that best fits on-board data was computed keeping into account the RDA measurements of range above the ground and terrain relative velocity.

Atmospheric reconstruction based on acceleration data is a viable solution where direct measurements are not possible. In this work, the inversion of the drag equation was used to retrieve the atmospheric density during the entry phase and then extended to the descent part of the mission adding the parachute effects. From the density both pressure and temperature profiles were computed integrating the hydrostatic equilibrium equation. In particular the assimilation of RDA data was crucial to fix the altitude and vertical velocity profiles, this in turn made possible to get realistic results.

The reconstructed atmospheric structure resulted in good agreement with the available model of the Martian atmosphere. Density, pressure and temperature during entry shown some zonal variations related to the trajectory of the DM. The derivation of atmospheric profiles during the descent phase resulted depend strongly on the DM dynamics particularly for the descent velocity as evidenced by uncertainty bounds. Indeed the profiles resulted again in good agreement with the models.

After the PDD the DM velocity became comparable with wind speed, the analysis of the local acceleration evidenced two winds fields that caused an off-vertical inclination of the DM around 6 km and 3 km above the ground. The latter event was confirmed by RDA direct measurements. The wind directed to south, south-west is compatible with the hook shaped ground track as well as the position of the parachute and the back-cover evidenced on landing site images.

Acknowledgements This work was supported by Italian Space Agency (ASI) in the framework of the ExoMars 2016 project – AMELIA experiment (ASI grant n. 2017-03-17 and n. I/018/12/3) and by the University of Padova. The authors are extremely grateful to Stefano Portigliotti from Thales Alenia Space Italy for his valuable help in understanding the operation of Schiaparelli EDL system and for the validation of AMELIA simulations. They wish to thank Andrew Ball and Leila Lorenzoni from ESA for their support in retrieving key informations for the final outcome of the analysis. They wish also to thank Davide Bonetti from Deimos Space for providing important clarifications on RDA measurements.

Appendix A: Equations of Motion

Let be M the inertial MMED reference frame and G the GNC body frame. The EDM state is defined as follows

$$\boldsymbol{x} = \left[{}^{\mathrm{M}}\boldsymbol{v}\ {}^{\mathrm{G}}\boldsymbol{q}_{\mathrm{M}}\ {}^{\mathrm{M}}\boldsymbol{p}\right]^{T} \tag{A.1}$$

with the velocity and position expressed in Cartesian coordinates with respect to MMED frame and the attitude quaternion representing the transformation from the MMED frame to the GNC frame. In the following the used reference frames will be indicated only if needed.

We assume that both the acceleration ${}^{\mathrm{G}}\boldsymbol{a}$ and angular rate ${}^{\mathrm{G}}\boldsymbol{\omega}$ are given with respect to the GNC frame and are already compensated for offsets and biases. This results in the following set of equations

$$\frac{d}{dt}\begin{bmatrix}\boldsymbol{v}\\ \boldsymbol{q}\\ \boldsymbol{p}\end{bmatrix}=\begin{bmatrix}\boldsymbol{a}_g+\boldsymbol{C}^T(\boldsymbol{q})\,\boldsymbol{a}\\ \boldsymbol{K}(\boldsymbol{q})\,\boldsymbol{\omega}\\ \boldsymbol{v}\end{bmatrix} \tag{A.2}$$

where $\boldsymbol{C}(\boldsymbol{q})$ is the rotation matrix corresponding to the attitude quaternion, $\boldsymbol{K}(\boldsymbol{q})$ is the quaternion kinematic matrix and $\boldsymbol{a}_g$ is the gravitational acceleration. The quaternion is composed by a scalar and vectorial part $\boldsymbol{q}=[\boldsymbol{q}_v q_s]^T$ and then

$$\boldsymbol{C}(\boldsymbol{q})=\boldsymbol{I}-2q_sS(\boldsymbol{q}_v)+2S(\boldsymbol{q}_v)S(\boldsymbol{q}_v) \tag{A.3}$$

$$\boldsymbol{K}(\boldsymbol{q})=\frac{1}{2}\begin{bmatrix}q_s\boldsymbol{I}+S(\boldsymbol{q}_v)\\ -\boldsymbol{q}_v^T\end{bmatrix} \tag{A.4}$$

with the cross-product, skew-symmetric matrix operator S defined as

$$S(\boldsymbol{x})=\begin{bmatrix}0 & -x_3 & x_2\\ x_3 & 0 & -x_1\\ -x_2 & x_1 & 0\end{bmatrix} \tag{A.5}$$

refer to Shuster (1993) for more details.

Inertial measurements are modeled using additive Gaussian white noise

$${}^{\mathrm{G}}\boldsymbol{y}_\omega={}^{\mathrm{G}}\boldsymbol{w}+\boldsymbol{\epsilon}_\omega \tag{A.6}$$

$${}^{\mathrm{G}}\boldsymbol{y}_a={}^{\mathrm{G}}\boldsymbol{a}+\boldsymbol{\epsilon}_a \tag{A.7}$$

hence the best available estimate of the acceleration and angular rate to be used in Eq. (A.2) and Eq. (A.14) are the measurements itself $\widehat{\boldsymbol{a}}=\boldsymbol{y}_a$ and $\widehat{\boldsymbol{\omega}}=\boldsymbol{y}_\omega$.

Velocity and position are modeled using additive errors

$$\boldsymbol{v}=\widehat{\boldsymbol{v}}+\boldsymbol{\delta}_v \tag{A.8}$$

$$\boldsymbol{p}=\widehat{\boldsymbol{p}}+\boldsymbol{\delta}_p \tag{A.9}$$

Since a quaternion is by definition unit length its covariance matrix is singular hence, to avoid numerical problems, a small angle multiplicative model is used (Lefferts et al. 1982; Markley 2003). The Rotation from MMED to GNC frame is represented as the composition of two consecutive rotations

$${}^{\mathrm{G}}\boldsymbol{q}_{\mathrm{M}}={}^{\mathrm{G}}\boldsymbol{q}_{\widehat{\mathrm{G}}}\otimes{}^{\widehat{\mathrm{G}}}\boldsymbol{q}_{\mathrm{M}}=\boldsymbol{\delta}_q\otimes{}^{\widehat{\mathrm{G}}}\boldsymbol{q}_{\mathrm{M}} \tag{A.10}$$

the first quaternion rotates from inertial M to estimated body frame $\widehat{G}$ the second quaternion rotates from the estimated body frame $\widehat{G}$ to the true body frame G. Since the first rotation is very small we can approximate the error quaternion $\boldsymbol{\delta}_q$ with a 3×1 error angle vector $\boldsymbol{\delta}_\theta$ as follow

$$\boldsymbol{\delta}_q=\begin{bmatrix}\boldsymbol{u}\sin(\delta_\theta/2)\\ cos(\delta_\theta/2)\end{bmatrix}\approx\begin{bmatrix}\frac{1}{2}\boldsymbol{\delta}_\theta\\ 1\end{bmatrix} \tag{A.11}$$

with $\boldsymbol{u}$, $\|\boldsymbol{u}\| = 1$ the rotation axis and δ_θ the rotation angle. In this hypothesis the corresponding rotation matrix results

$$\boldsymbol{C}(\boldsymbol{\delta}_q) \approx \boldsymbol{I} - S(\boldsymbol{\delta}_\theta) \tag{A.12}$$

The state error is defined as $\boldsymbol{\delta}_x = [\boldsymbol{\delta}_v \boldsymbol{\delta}_\theta \boldsymbol{\delta}_p]^T$ and evolves according to the following equation

$$\frac{d}{dt}\boldsymbol{\delta}_x = \boldsymbol{A}\,\boldsymbol{\delta}_x + \boldsymbol{B}\,\boldsymbol{\epsilon} + \boldsymbol{\eta} \tag{A.13}$$

where $\boldsymbol{A}$ is the Jacobian of the state equation (A.2) with respect to the state $\boldsymbol{x}$ and $\boldsymbol{B}$ is the Jacobian with respect to the input noise $\boldsymbol{\epsilon} = [\boldsymbol{\epsilon}_\omega \boldsymbol{\epsilon}_a]^T$ and $\boldsymbol{\eta} = [\boldsymbol{\eta}_v \boldsymbol{\eta}_\theta \boldsymbol{\eta}_p]$ is the state error modeled as Gaussian white noise. The corresponding system of equations reads as

$$\frac{d}{dt}\begin{bmatrix}\boldsymbol{\delta}_v\\ \boldsymbol{\delta}_\theta\\ \boldsymbol{\delta}_p\end{bmatrix} = \begin{bmatrix}0 & -\boldsymbol{C}^T(\boldsymbol{q})S(\boldsymbol{a}) & 0\\ 0 & -S(\boldsymbol{\omega}) & 0\\ \boldsymbol{I} & 0 & 0\end{bmatrix}\begin{bmatrix}\boldsymbol{\delta}_v\\ \boldsymbol{\delta}_\theta\\ \boldsymbol{\delta}_p\end{bmatrix} + \begin{bmatrix}0 & \boldsymbol{C}^T(\boldsymbol{q})\\ \boldsymbol{I} & 0\\ 0 & 0\end{bmatrix}\begin{bmatrix}\boldsymbol{\epsilon}_\omega\\ \boldsymbol{\epsilon}_a\end{bmatrix} + \begin{bmatrix}\boldsymbol{\eta}_v\\ \boldsymbol{\eta}_\theta\\ \boldsymbol{\eta}_p\end{bmatrix} \tag{A.14}$$

note that the effects of uncertainties on the gravitational acceleration are assumed to be negligible. The corresponding first order state covariance $\boldsymbol{P}$ is a 9×9 matrix computed integrating the following continuous time equation

$$\frac{d}{dt}\boldsymbol{P} = \boldsymbol{A}\boldsymbol{P} + \boldsymbol{P}\boldsymbol{A}^T + \boldsymbol{B}\boldsymbol{Q}\boldsymbol{B}^T + \boldsymbol{R} \tag{A.15}$$

with $\boldsymbol{Q}$ and $\boldsymbol{R}$ respectively the input and state noise covariance matrices.

Appendix B: RDA Measurements Model

RDA had four beams oriented as shown in Fig. 1, the sensing direction of each beam is represented by the constant versors ${}^{\mathrm{G}}\boldsymbol{s}_n$, $n = 0, 1, 2, 3$. Assuming a flat horizontal surface as described Sect. 7, the slant-range and slant-out measurements correspond to the distance in meters along the beam from the centre of GNC frame to the plane below the DM at the altitude h AGL. The altitude AGL is computed from the position vector $\boldsymbol{p}$ as

$$h = \|\boldsymbol{p}\| - r_{\mathrm{MOLA}} - r_{\mathrm{GROUND}} \tag{B.1}$$

with constant $r_{\mathrm{MOLA}} = 3396000$ m and $r_{\mathrm{GROUND}} = -1440$ m. The rotation from the GNC frame to the local NED frame is ${}^{\mathrm{N}}\boldsymbol{C}_{\mathrm{G}} = {}^{\mathrm{N}}\boldsymbol{C}_{\mathrm{M}}\,{}^{\mathrm{M}}\boldsymbol{C}_{\mathrm{G}}$, where the first rotation from the MMED to the local NED frame ${}^{\mathrm{N}}\boldsymbol{C}_{\mathrm{M}}$ depends on the DM position and the second rotation is computed using the attitude quaternion. Expressing the beam direction with respect to the local NED reference frame, the Z component of the versor reads as

$$z_n = \boldsymbol{e}_{\mathrm{Z}}\,{}^{\mathrm{N}}\boldsymbol{C}_{\mathrm{M}}\,\boldsymbol{C}^T(\boldsymbol{q})\,\boldsymbol{s}_n \tag{B.2}$$

with $\boldsymbol{e}_{\mathrm{Z}} = [0\,0\,1]$. The ${}^{\mathrm{N}}\boldsymbol{C}_{\mathrm{M}}$ is computed using the estimated position but it is considered constant in the derivation of the error model. The slant-range measurement model is simply

$$y_{s,n} = \frac{h}{z_n} = \frac{\|\boldsymbol{p}\| - r_{\mathrm{MOLA}} - r_{\mathrm{GROUND}}}{\boldsymbol{e}_{\mathrm{Z}}\,{}^{\mathrm{N}}\boldsymbol{C}_{\mathrm{M}}\,\boldsymbol{C}^T(\boldsymbol{q})\,\boldsymbol{s}_n} \tag{B.3}$$

note that Eq. (B.2) and hence this equation are invariant for rotations along the local vertical, this issue is considered in the implementation of the estimator as discussed in Sect. 8. The slant-range error model is then

$$\delta_{y_{s,n}} = \boldsymbol{H}_{s,n}\,\boldsymbol{\delta}_x + \epsilon_{s,n} = \begin{bmatrix} \mathbf{0} & \frac{h}{z_n^2}\,\boldsymbol{e}_Z{}^{\mathrm{N}}\boldsymbol{C}_{\mathrm{M}}\,\boldsymbol{C}^T(\boldsymbol{q})\,S(\boldsymbol{s}_n) & \frac{1}{z_n\,\|\boldsymbol{p}\|}\,\boldsymbol{p}^{\mathrm{T}} \end{bmatrix} \begin{bmatrix} \boldsymbol{\delta}_v \\ \boldsymbol{\delta}_\theta \\ \boldsymbol{\delta}_p \end{bmatrix} + \epsilon_{s,n} \tag{B.4}$$

where $\epsilon_{s,n}$ is the uncertainty in the slant range measurement of each beam; measurement uncertainties were modeled as Gaussian white noise. To model the slant-out measurements we used only the B0 model $y_{s,0}$ while the slant-range is derived stacking the equations related to B0, B1, B2 and B3 in a vector $\boldsymbol{y}_s = [y_{s,0}\ y_{s,1}\ y_{s,2}\ y_{s,3}]^T$.

The terrain relative velocity was determined independently along each RDA beam (Bombaci et al. 2016) and then processed on-board to get the co-rotating velocity of the DM expressed in the GNC reference frame. The velocity-out measurements are modeled expressing the DM terrain relative velocity in the MMED frame by means of the state variables in Eq. (A.1) and then rotating this velocity to the GNC. This reads as

$$\boldsymbol{y}_v = \boldsymbol{C}(\boldsymbol{q})\,(\boldsymbol{v} - \boldsymbol{\Omega}\,\boldsymbol{p}) \tag{B.5}$$

where $\boldsymbol{\Omega} = S(\boldsymbol{w}_{\mathrm{MARS}})$ and $\boldsymbol{w}_{\mathrm{MARS}}$ is the angular rate of Mars. The corresponding error model is

$$\delta_{y_v} = \boldsymbol{H}_v\,\boldsymbol{\delta}_x + \boldsymbol{\epsilon}_v = \begin{bmatrix} \boldsymbol{C}(\boldsymbol{q}) & \boldsymbol{C}(\boldsymbol{q})\,S(\boldsymbol{v} - \boldsymbol{\Omega}\,\boldsymbol{p})\boldsymbol{C}^T(\boldsymbol{q}) & -\boldsymbol{C}(\boldsymbol{q})\,\boldsymbol{\Omega} \end{bmatrix} \begin{bmatrix} \boldsymbol{\delta}_v \\ \boldsymbol{\delta}_\theta \\ \boldsymbol{\delta}_p \end{bmatrix} + \boldsymbol{\epsilon}_v \tag{B.6}$$

with $\boldsymbol{\epsilon}_v$ the uncertainty in the velocity estimate; measurement uncertainties were modeled as Gaussian white noise.

References

A. Aboudan, G. Colombatti, F. Ferri, F. Angrilli, Huygens probe entry trajectory and attitude estimated simultaneously with Titan atmospheric structure by Kalman filtering. Planet. Space Sci. **56**(5), 573–585 (2008). https://doi.org/10.1016/j.pss.2007.10.006. http://www.sciencedirect.com/science/article/pii/S0032063307003479. Titan as seen from Huygens—Part 2

C. Bettanini, F. Esposito, S. Debei, C. Molfese, G. Colombatti, A. Aboudan, J. Brucato, F. Cortecchia, G.D. Achille, G. Guizzo, E. Friso, F. Ferri, L. Marty, V. Mennella, R. Molinaro, P. Schipani, S. Silvestro, R. Mugnuolo, S. Pirrotta, E. Marchetti, A.M. Harri, F. Montmessin, C. Wilson, I.A. Rodríguez, S. Abbaki, V. Apestigue, G. Bellucci, J.J. Berthelier, S. Calcutt, F. Forget, M. Genzer, P. Gilbert, H. Haukka, J. Jiménez, S. Jiménez, J.L. Josset, O. Karatekin, G. Landis, R. Lorenz, J. Martinez, D. Möhlmann, D. Moirin, E. Palomba, M. Patel, J.P. Pommereau, C. Popa, S. Rafkin, P. Rannou, N. Renno, W. Schmidt, F. Simoes, A. Spiga, F. Valero, L. Vázquez, F. Vivat, O. Witasse, The DREAMS experiment flown on the ExoMars 2016 mission for the study of Martian environment during the dust storm season. Measurement **122**, 484–493 (2018). https://doi.org/10.1016/j.measurement.2018.01.019. http://www.sciencedirect.com/science/article/pii/S0263224118300186

R.C. Blanchard, P.N. Desai, Mars Phoenix entry, descent, and landing trajectory and atmosphere reconstruction. J. Spacecr. Rockets **48**(5), 809–822 (2011). https://doi.org/10.2514/1.46274

O. Bombaci, M. Iorio, P. Pepe, Exomars radar Doppler altimeter (a Doppler radar for accurate attitude measurements in support to landing phase), in *2016 IEEE Metrology for Aerospace (MetroAeroSpace)* (2016), pp. 65–70. https://doi.org/10.1109/MetroAeroSpace.2016.7573187

D. Bonetti, G. De Zaiacomo, G. Blanco Arnao, I. Pontijas Fuentes, S. Portigliotti, L. Lorenzoni, O. Bayle, Exomars 2016 post flight mission analysis of Schiaparelli coasting, entry, descent and landing, in *14th International Planetary Probe Workshop IPPW*, The Hague, The Netherlands, June 2017

A. Chen, A. Cianciolo, A.R. Vasavada, C. Karlgaard, J. Barnes, B. Cantor, D. Kass, S. Rafkin, D. Tyler, Reconstruction of atmospheric properties from Mars Science Laboratory entry, descent, and landing. J. Spacecr. Rockets **51**(4), 1062–1075 (2014). https://doi.org/10.2514/1.A32708

G. Colombatti, P. Withers, F. Ferri, A. Aboudan, A. Ball, C. Bettanini, V. Gaborit, A. Harri, B. Hathi, M. Leese, T. Makinen, P. Stoppato, M. Towner, J. Zarnecki, F. Angrilli, M. Fulchignoni, Reconstruction of the trajectory of the Huygens probe using the Huygens Atmospheric Structure Instrument (HASI). Planet. Space Sci. **56**(5), 586–600 (2008). https://doi.org/10.1016/j.pss.2007.11.017. http://www.sciencedirect.com/science/article/pii/S0032063307003480. Titan as seen from Huygens—Part 2

F. Esposito et al., The DREAMS experiment onboard the Schiaparelli module of the ExoMars 2016 mission: design, performances and expected results. Space Sci. Rev. (2018, in press)

F. Ferri, et al., ExoMars Atmospheric Mars Entry and Landing Investigations and Analysis (AMELIA). Space Sci. Rev. (2018, in press)

F. Forget, F. Hourdin, R. Fournier, C. Hourdin, O. Talagrand, M. Collins, S.R. Lewis, P.L. Read, J.P. Huot, Improved general circulation models of the Martian atmosphere from the surface to above 80 km. J. Geophys. Res., Planets **104**(E10), 24,155–24,175 (1999). https://doi.org/10.1029/1999JE001025

A. Gulhan, T. Thiele, F. Siebe, R. Kronen, Combined instrumentation package COMARS+ for the ExoMars Schiaparelli lander. Space Sci. Rev. **214**(1), 12 (2017). https://doi.org/10.1007/s11214-017-0447-4

C. Holstein-Rathlou, A. Maue, P. Withers, Atmospheric studies from the Mars Science Laboratory entry, descent and landing atmospheric structure reconstruction. Planet. Space Sci. **120**, 15–23 (2016). https://doi.org/10.1016/j.pss.2015.10.015. http://www.sciencedirect.com/science/article/pii/S0032063315003207

C.D. Karlgaard, P. Kutty, M. Schoenenberger, M.M. Munk, A. Little, C.A. Kuhl, J. Shidner, Mars Science Laboratory entry atmospheric data system trajectory and atmosphere reconstruction. J. Spacecr. Rockets **51**(4), 1029–1047 (2014). https://doi.org/10.2514/1.A32770

B. Kazeminejad, D. Atkinson, M. Pérez-Ayúcar, J. Lebreton, C. Sollazzo, Huygens' entry and descent through Titan's atmosphere: methodology and results of the trajectory reconstruction. Planet. Space Sci. **55**(13), 1845–1876 (2007). https://doi.org/10.1016/j.pss.2007.04.013. http://www.sciencedirect.com/science/article/pii/S0032063307001171. Titan as seen from Huygens

E.J. Lefferts, F.L. Markley, M.D. Shuster, Kalman filtering for spacecraft attitude estimation. J. Guid. Control Dyn. **5**(5), 417–429 (1982). https://doi.org/10.2514/3.56190

J.A. Magalhães, J.T. Schofield, A. Seiff, Results of the Mars Pathfinder atmospheric structure investigation. J. Geophys. Res., Planets **104**(E4), 8943–8955 (1999). https://doi.org/10.1029/1998JE900041

L. Markley, Attitude error representations for Kalman filtering. J. Guid. Control Dyn. **26**(2), 311–317 (2003). https://doi.org/10.2514/2.5048

E. Millour, F. Forget, A. Spiga, T. Navarro, J.B. Madeleine, L. Montabone, F. Lefevre, F. Montmessin, J.Y. Chaufray, M. Lopez-Valverde, F. Gonzalez-Galindo, S. Lewis, P. Read, J.P. Huot, M.C. Desjean, The Mars Climate Database (MCD version 2.5), in *EPSC2015-438*, vol. 10 (2015)

S. Portigliotti, C. Cassi, M. Montagna, P. Martella, M. Faletra, S. De Sanctis, D. Granà, O. Bayle, T. Blancquaert, L. Lorenzoni, ExoMars 2016, the Schiaparelli mission. EDL demonstration results from real time telemetry before unfortunate impact, in *14th International Planetary Probe Workshop IPPW*, The Hague, The Netherlands, June 2017

S. Särkkä, *Bayesian Filtering and Smoothing. Institute of Mathematical Statistics Textbooks* (Cambridge University Press, Cambridge, 2013). https://books.google.it/books?id=5VlsAAAAQBAJ

A. Seiff, Mars atmospheric winds indicated by motion of the Viking landers during parachute descent. J. Geophys. Res., Planets **98**(E4), 7461–7474 (1993). https://doi.org/10.1029/92JE02738

M.D. Shuster, A survey of attitude representations. J. Astronaut. Sci. **41**(4), 439–517 (1993)

D.E. Smith, M.T. Zuber, H.V. Frey, J.B. Garvin, J.W. Head, D.O. Muhleman, G.H. Pettengill, R.J. Phillips, S.C. Solomon, H.J. Zwally, W.B. Banerdt, T.C. Duxbury, M.P. Golombek, F.G. Lemoine, G.A. Neumann, D.D. Rowlands, O. Aharonson, P.G. Ford, A.B. Ivanov, C.L. Johnson, P.J. McGovern, J.B. Abshire, R.S. Afzal, X. Sun, Mars Orbiter Laser Altimeter: experiment summary after the first year of global mapping of Mars. J. Geophys. Res., Planets **106**(E10), 23,689–23,722 (2001). https://doi.org/10.1029/2000JE001364

D.A. Spencer, R.C. Blanchard, R.D. Braun, P.H. Kallemeyn, S.W. Thurman, Mars Pathfinder entry, descent, and landing reconstruction. J. Spacecr. Rockets **36**(3), 357–366 (1999). https://doi.org/10.2514/2.3478

T. Tolker-Nielsen, ExoMars 2016—Schiaparelli anomaly inquiry. Report DG-I/2017/546/TTN Iss. 1, Rev. 0, ESA (2017)

J. Vago, O. Witasse, H. Svedhem, P. Baglioni, A. Haldemann, G. Gianfiglio, T. Blancquaert, D. McCoy, R. de Groot, ESA ExoMars program: the next step in exploring Mars. Sol. Syst. Res. **49**(7), 518–528 (2015). https://doi.org/10.1134/S0038094615070199

J. Wertz, *Spacecraft Attitude Determination and Control*. Astrophysics and Space Science Library (Springer, Netherlands, 1978). https://books.google.it/books?id=GtzzpUN8VEoC

P. Withers, A smoothing technique for improving atmospheric reconstruction for planetary entry probes. Planet. Space Sci. **79–80**, 52–55 (2013). https://doi.org/10.1016/j.pss.2013.01.011. http://www.sciencedirect.com/science/article/pii/S0032063313000263

P. Withers, D.C. Catling, Observations of atmospheric tides on Mars at the season and latitude of the Phoenix atmospheric entry. Geophys. Res. Lett. **37**(24), l24204 (2010). https://doi.org/10.1029/2010GL045382

P. Withers, M.D. Smith, Atmospheric entry profiles from the Mars Exploration Rovers Spirit and Opportunity. Icarus **185**(1), 133–142 (2006). https://doi.org/10.1016/j.icarus.2006.06.013. http://www.sciencedirect.com/science/article/pii/S0019103506002302